Annales Geophysicae (2003) 21: 1723–1736 © European Geosciences Union 2003

Annales Geophysicae

A quantitative model of the planetary Na^+ contribution to Mercury's magnetosphere

D. C. Delcourt[1], **S. Grimald**[1], **F. Leblanc**[2], **J.-J. Berthelier**[1], **A. Millilo**[3], **A. Mura**[3], **S. Orsini**[3], **and T. E. Moore**[4]

[1]CETP-CNRS, Saint-Maur des Fossés, France
[2]Service d'Aéronomie-CNRS, Verrières-le-Buisson, France
[3]IFSI-CNR, Roma, Italy
[4]NASA-GSFC, Greenbelt, USA

Received: 5 November 2002 – Revised: 28 March 2003 – Accepted: 8 April 2003

Abstract. We examine the circulation of heavy ions of planetary origin within Mercury's magnetosphere. Using single particle trajectory calculations, we focus on the dynamics of sodium ions, one of the main species that are ejected from the planet's surface. The numerical simulations reveal a significant population in the near-Mercury environment in the nightside sector, with energetic (several keV) Na^+ densities that reach several tenths cm^{-3} at planetary perihelion. At aphelion, a lesser (by about one order of magnitude) density contribution is obtained, due to weaker photon flux and solar wind flux. The numerical simulations also display several features of interest that follow from the small spatial scales of Mercury's magnetosphere. First, in contrast to the situation prevailing at Earth, ions in the magnetospheric lobes are found to be relatively energetic (a few hundreds of eV), despite the low-energy character of the exospheric source. This results from enhanced centrifugal acceleration during $\boldsymbol{E} \times \boldsymbol{B}$ transport over the polar cap. Second, the large Larmor radii in the mid-tail result in the loss of most Na^+ into the dusk flank at radial distances greater than a few planetary radii. Because gyroradii are comparable to, or larger than, the magnetic field variation length scale, the Na^+ motion is also found to be non-adiabatic throughout most of Mercury's equatorial magnetosphere, leading to chaotic scattering into the loss cone or meandering (Speiser-type) motion in the near-tail. As a direct consequence, a localized region of energetic Na^+ precipitation develops at the planet's surface. In this region which extends over a wide range of longitudes at mid-latitudes ($\sim$30°–40°), one may expect additional sputtering of planetary material.

Key words. Magnetospheric physics (planetary magnetospheres) – Space plasma physics (charged particle motion and acceleration; numerical simulation studies)

Correspondence to: D. C. Delcourt
(dominique.delcourt@cetp.ipsl.fr)

1 Introduction

Mariner-10 observations in 1974 and 1975 have revealed an intrinsic magnetic field at Mercury, with a reduced (by about 2 orders of magnitude) dipolar moment as compared to that of Earth. The spatial and temporal scales of the resulting magnetosphere differ widely from those of the terrestrial magnetosphere, by factors of about 8 and 40, respectively. Measurements by the forthcoming Messenger and Bepi Colombo missions to Mercury will allow for in-depth analysis of a number of physical phenomena that have been partly unveiled by Mariner-10. Detailed comparison with observations in the terrestrial magnetosphere will provide a better understanding of these phenomena on different scales. For example, it is not clear whether the energetic electron injections recorded by Mariner-10 are due to magnetic flux pile-up and internal instabilities as observed during substorms at Earth (e.g. Baker et al., 1986; Christon et al., 1987; Taktakishvili and Zelenyi, 1988) or to direct coupling with the solar wind (e.g. Luhmann et al., 1998). In fact, the actual structure of Mercury's magnetosphere and the existence of large-scale plasma cells (e.g. lobe, plasma sheet, and boundary layers), as in the case of the Earth's magnetosphere, remain to be elucidated. In this regard, one of the key issues that is still controversial to date in magnetospheric physics has to do with the role of the internal plasma source (e.g. the terrestrial ionosphere) versus that of the solar wind in the overall magnetospheric structure and dynamics. At Earth, several studies have shown that ionospheric ion outflows depend strongly on geomagnetic activity, as well as solar wind dynamic pressure (e.g. Yau et al., 1985; Moore et al., 1999). It is also well established that these populations can significantly contribute to the ring current, thus playing a key role during the main phase of magnetic storms (e.g. Hamilton et al., 1988; Daglis and Axford, 1996). At Mercury, numerical simulations suggest that the solar wind may gain access to the inner magnetosphere as well (e.g. Kallio and Janhunen, 2003), and one may wonder about the development of magnetic storms if the internal plasma source is reduced (e.g. Moore et al., 2001).

The purpose of the present study is to investigate the transport of ions of planetary origin in Mercury's magnetosphere. We use three-dimensional, single-particle trajectory calculations to track the behavior of Na^+ ions, one of the major species that is ejected from the planet's surface (e.g. Potter and Morgan, 1985; Killen et al., 2001). Our intent is to derive first-order estimates of their contribution to Mercury's magnetosphere. Within the limits of the model, we show that the density deposited by these ions may be quite significant (several tenths cm^{-3}) at perihelion, whereas somewhat reduced values are obtained at aphelion. In Sect. 2, we first review some features of nonlinear particle dynamics that are of importance at Mercury. The Na^+ contribution to the magnetosphere is then discussed in Sect. 3, whereas Sect. 4 is dedicated to ions that impact the planet's surface.

2 Model particle orbits

In order to investigate the magnetospheric transport of ions originating from the exosphere, we performed test particle simulations in three-dimensional electric and magnetic field models that provide a first-order description of Mercury's environment. For the magnetic field, following the analysis of Ip (1987), we adopt the simple model of Luhmann and Friesen (1979). This model consists of the superposition of an internal dipole field and an infinite Harris sheet. Assuming the dipole field to be untilted, and denoting the radial distance by R, the azimuth by φ, and the latitude by λ, one has in spherical coordinates:

$$B_R = -2\frac{M}{R^3}\sin\lambda - B_T \tanh\frac{Z}{L}\cos\varphi\cos\lambda \tag{1a}$$

$$B_\varphi = B_T \tanh\frac{Z}{L}\sin\varphi \tag{1b}$$

$$B_\lambda = \frac{M}{R^3}\cos\lambda + B_T \tanh\frac{Z}{L}\cos\varphi\sin\lambda \tag{1c}$$

where M is the dipole moment, B_T, the asymptotic tail field, and L, the current sheet half-thickness. Luhmann and Friesen (1979) demonstrated that this simple model reproduces essential features of the Earth's magnetosphere. Note that the magnetopause here is not explicitly specified and may be identified by tracing the outermost field lines that are connected to the planet's surface. Unlike the modified version of the Tsyganenko (1996) model that was used in recent studies (e.g. Luhmann et al., 1998; Massetti et al., 2002), Eqs. (1a)–(1c) do not allow us to explore in detail the magnetosphere's structure and its variations due to changes in the interplanetary magnetic field (IMF) parameters (e.g. Goldstein et al., 1981; Kabin et al., 2000). However, Eqs. (1a)–(1c) provide a good first-order description of Mercury's environment, which allows us to trace a large number of test particles. Specifically, with $M = 385\,\mathrm{nT}.R_M^3$, $B_T = 100\,\mathrm{nT}$, and $L = 500\,\mathrm{km}$ in Eqs. (1a)–(1c), one obtains a magnetospheric topology that is roughly consistent with that derived from Mariner-10 measurements (e.g. Whang, 1977). In particular, the magnetospheric volume occupied by the planet is much larger at Mercury than at Earth, and the subsolar point lies fairly close to the planet's surface, at about $1.4\,R_M$ (see, e.g. Fig. 2, introduced later).

As for the electric field, a coupling process similar to that at Earth is expected to occur at Mercury, with reconnection of IMF and magnetospheric field lines in the frontside sector and subsequent transport into the antisunward direction over the polar cap. In the terrestrial magnetosphere, this convection process goes together with a current system that closes through the ionosphere. At Mercury, this cannot be the case because of the absence of such an ionosphere, and processes responsible for current closure to date remain controversial (e.g. Glassmeier, 1997). Still, to account for antisunward convection of the magnetic field lines over the polar cap and because prescribing a convection electric field in the equatorial plane (e.g. Roederer, 1970) does not allow for investigation of the lobe region, we were led to consider as a first approximation the Volland (1978) formulation originally devised for ionospheric plasma flow at Earth. Accordingly, a two-cell pattern of potential distribution has been imposed at the planet's surface, with antisunward transport at high latitudes (above $\sim 48°$ invariant latitude with the above magnetic field parameters) and sunward transport below. Regarding the cross-polar cap potential drop, the distance over which magnetospheric field lines are reconnected with the IMF is obviously smaller at Mercury than at Earth. On the other hand, due to magnetic flux conservation, the IMF magnitude at Mercury is larger (by about a factor 4) than at 1 AU, hence producing a larger reconnection-associated electric field. In the present calculations, we considered average values of the solar wind speed ($\sim$400 km s^{-1}) and IMF magnitude ($\sim$30 nT), and set the cross-polar cap potential drop to 20 kV, which leads to a dawn-to-dusk electric field of $\sim 2\,\mathrm{mV\,m^{-1}}$ in the central magnetotail (see, e.g. Eq. (5) of Ip, 1987). Once the magnetic and electric field models were prescribed, the perpendicular electric field components at a given point of the magnetosphere were calculated by assuming that the magnetic field lines are equipotentials and by integrating neighboring field lines down the planet's surface (e.g. Delcourt et al., 1989).

The test particle trajectories were computed using the full equation of motion. As mentioned above, Mercury's magnetosphere is much smaller than the terrestrial one, so that ions are likely to exhibit Larmor radii comparable to the length scale of field variations. This invalidates an adiabatic (guiding center based) treatment (e.g. Northrop, 1963). As a matter of fact, as will be seen later, the numerical simulations reveal that at Mercury, non-adiabatic effects are of crucial importance for most of the ion magnetospheric transport. A parameter that is widely used to characterize such a nonadiabatic behavior is the parameter κ, defined as the square root of the minimum field line curvature radius to maximum Larmor radius ratio (Büchner and Zelenyi, 1989). In the magnetotail, this adiabaticity parameter is calculated at the equator, where the magnetic field magnitude

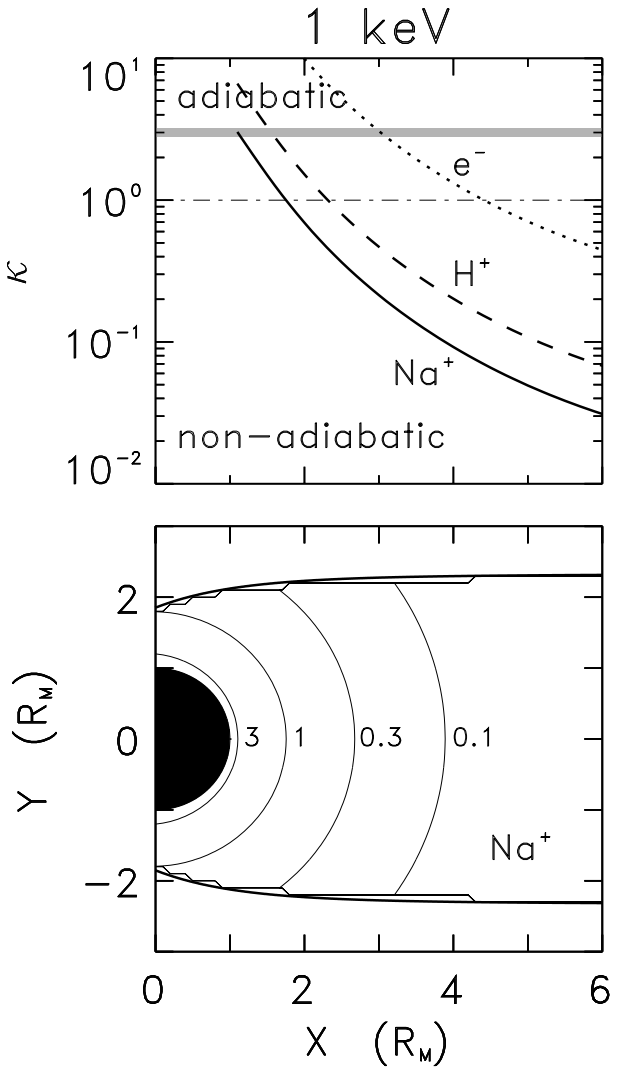

Fig. 1. (top) Variation of the adiabaticity parameter κ as a function of radial distance along the tail axis. Solid, dashed, and dotted lines correspond to Na^+ ions, protons, and electrons with 1 keV energy, respectively. (bottom) Contours of the κ parameter in the equatorial plane. Here, only 1 keV Na^+ are considered.

is minimum. For $\kappa > 3$, the particle motion is adiabatic (equivalently, magnetic moment conserving). As κ decreases from 3 toward unity, magnetic moment scattering affects particles with increasingly larger pitch angles at the equator (see, e.g. Fig. 1 of Delcourt et al., 1996). This latter behavior may be viewed as the result of a perturbation of the particle gyromotion by an impulsive centrifugal force near the field minimum (Delcourt et al., 1994).

For $\kappa < 1$, particles experience a fast oscillation about the midplane while slowly gyrating around the small magnetic field component normal to the midplane. In particular, in this latter κ range, particles may execute so-called Speiser-type orbits (Speiser, 1965), where they meander inside the equatorial current sheet and subsequently escape with a magnetic moment nearly identical to that at entry; hence, their denomination as quasi-adiabatic, though it is not adiabatic stricto sensu (Büchner and Zelenyi, 1989). Chen and Palmadesso (1986) noted that such a Speiser-type behavior is obtained preferentially for specific κ values (smaller than 1), which was interpreted to result from resonance between the fast meandering motion and the slow gyromotion. These resonant dynamical regimes are of importance for the magnetotail structure and dynamics since, during the meandering sequence along the dawn-to-dusk convection electric field, particles are subjected to a large energization. A thin current sheet results and, due to the weak change of magnetic moment, particles subsequently travel back to their initial mirror point which can be on either side of the current sheet depending on the order of the resonance. Burkhart and Chen (1991) further investigated this κ ordering and put forward the following empirical relationship to characterize the i-th resonance (i being an integer ≥ 1)

$$\kappa_i \approx \frac{0.8}{i + 0.6}. \quad (2)$$

According to Eq. (2), the first Speiser-dominated regime is expected near $\kappa = 0.5$, the second near $\kappa = 0.3$, the third near $\kappa = 0.22$ and so forth. Conversely, away from these resonant κ intervals, particles are subjected to prominent pitch-angle scattering.

The top panel of Fig. 1 shows the variations of the κ parameter along the X axis in the above magnetic field model (Eq. 1). Note that, in this study, the X axis points toward the tail, and the Y axis points from dusk to dawn. As will be seen in the following, even though Na^+ ions produced by neutral photo-ionization initially have very low energies, they are rapidly accelerated up to several hundreds of eV or a few keV, so that an average energy of 1 keV at equator was chosen in Fig. 1. It can be seen in the top panel of this figure that Na^+ ions become non-adiabatic ($\kappa < 3$) in the immediate vicinity of the planet. The bottom panel of Fig. 1 shows contours of the κ parameter in the equatorial plane and reveals similar variations, regardless of longitude. It is clearly apparent from Fig. 1 that, for 1 keV Na^+ ions, the adiabatic domain nearly vanishes. The contours in the bottom panel also indicate that the 1–3 κ range extends between $\sim 1\ R_M$ and $\sim 2\ R_M$ radial distance, so that prominent magnetic moment scattering and consequent injection into the loss cone may occur fairly close to the planet. On the other hand, Fig. 1 shows that the first resonance ($\kappa \approx 0.5$) is to be expected near $2\ R_M$ radial distance. This situation widely differs from that prevailing at Earth, where Speiser-type orbits are not expected inside of $\sim$8–10 R_E. Not surprisingly, it can also be seen in the top panel of Fig. 1 that the adiabatic-nonadiabatic threshold moves further out if one considers smaller mass-to-charge ratios. On the whole, however, this threshold occurs fairly close to the planet, viz., $\sim 2\ R_M$ for 1 keV protons and $\sim 3\ R_M$ for 1 keV electrons.

Figure 2 shows an example of Na^+ trajectory calculations. In this figure, test ions were launched from the planet's surface with 1 eV energy and from different latitudes (65°, 70°, and 75°, coded in blue, green and red, respectively) on the

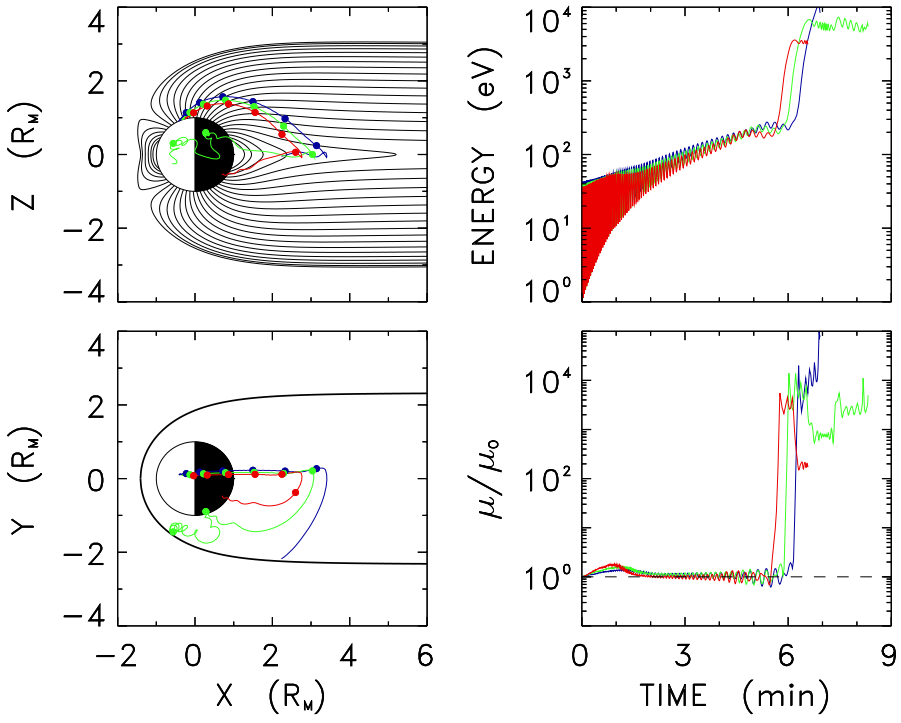

Fig. 2. Model Na^+ trajectories. Left panels show the trajectory projections (top) in the noon-midnight meridian plane and (bottom) in the equatorial plane. Right panels show (top) the particle kinetic energy and (bottom) the magnetic moment (normalized to the initial value) versus time. The ions are launched from the planet's surface at different latitudes (color-coded in blue, green, and red) in the dayside sector. Filled circles in the left panels show the time of flight in steps of one minute.

noon meridian. The left-hand panels of Fig. 2 present the Na^+ trajectory projections, the dots showing the time of flight in steps of one minute. It is apparent that the ions are rapidly (in a few minutes) transported from the high-latitude dayside sector into the near-tail. Subsequently, it can be seen that these ions experience a fast Z-oscillation about the midplane. Whereas the test ion launched from the lowest latitude (blue trajectory) rapidly intercepts the dusk magnetopause because of its large Larmor radius, the innermost Na^+ ion (red trajectory) displays a relatively weak change in magnetic moment after crossing the midplane (bottom right panel of Fig. 2) and returns to the strong B region at low altitudes, ultimately impacting the planet's surface. Further analysis of this latter orbit reveals that it approximately coincides with the second energy resonance, with $\kappa \approx 0.3$ (see, e.g. the bottom panel of Fig. 1). Finally, the trajectory shown in green in Fig. 2 depicts an intermediate situation, where the ion experiences a magnetic moment increase, mirrors at low altitude and subsequently intercepts the dayside magnetopause.

In the top right panel of Fig. 2, which shows the variations of the ion kinetic energy as a function of time, two main features may be noticed. First, it is apparent that substantial energization from a few eV up to a few hundreds of eV occurs during transport into the magnetospheric lobe. This follows from the centrifugal acceleration due to curvature of the $\boldsymbol{E} \times \boldsymbol{B}$ drift path as the particle convects over the polar cap (e.g. Cladis, 1986). At Mercury, this effect is enhanced because of the small spatial scales of the magnetosphere (Delcourt et al., 2002). Equivalently, the smaller the magnetospheric obstacle to the expanding solar wind is, the larger the centrifugal effect during convection from high to low latitudes. Second, as mentioned above, the meandering sequence about the midplane and the large duskward drift that goes with it yield prominent ion energization up to several keV. In other words, the ions that reimpact the planet or reach the magnetopause are far more energetic than at ejection into the magnetosphere. These large energy gains, together with the small spatial scale of the magnetosphere, make finite Larmor radius effects of paramount importance at Mercury. As a matter of fact, it will be seen in the following that most of the Na^+ ions that travel beyond $\sim 3\, R_M$ cannot gain access to the innermost region and are lost at the magnetopause.

3 Quantitative modeling of Na^+ contribution to the magnetosphere

To investigate the planetary Na^+ ion contribution to Mercury's magnetosphere, we performed systematic test particle trajectory computations, using as initial conditions Monte Carlo simulations of Mercury's exosphere. Different processes of Na production were considered in these latter simulations, namely photo-stimulated desorption and micrometeoritic vaporization. Sputtering due to the impinging

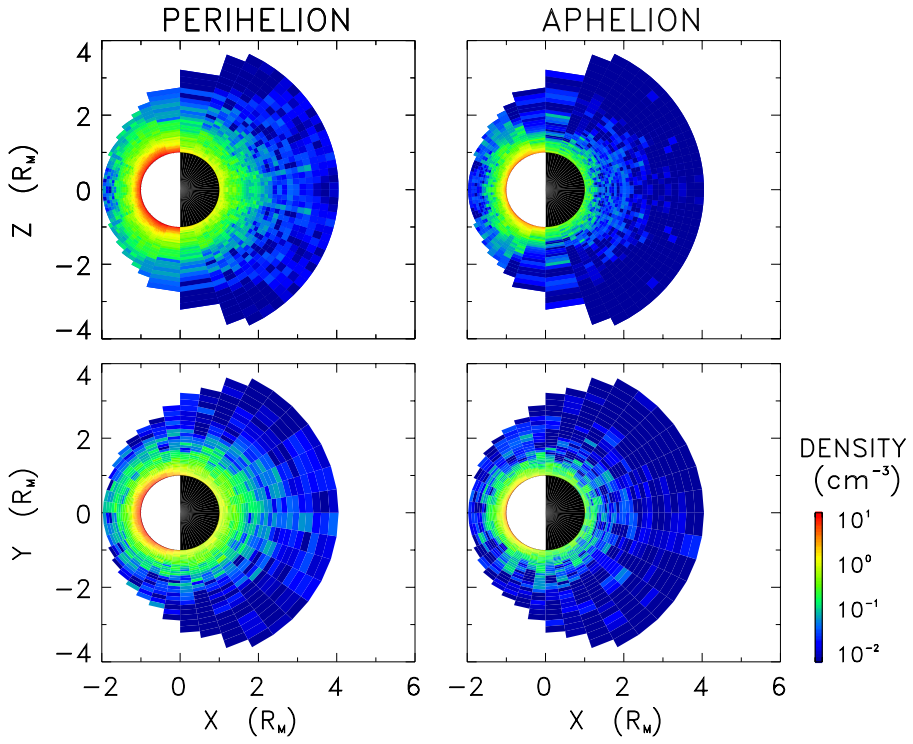

Fig. 3. Model density of sodium atoms at (left) Mercury's perihelion and (right) aphelion. Top and bottom panels show cross sections in the noon-midnight meridian plane and the equatorial plane, respectively. The density is coded according to the color scale at the right.

solar wind was also taken into account in the open field line region at high latitudes (above 50° invariant latitude) in the dayside sector. Neither thermal desorption nor competition between ejection processes have been considered in the simulations, which are a simplified version of the Leblanc and Johnson (2002) model. This is done to simplify our work and is justified because thermal desorption produces only low energy (less than 0.05 eV) sodium ejecta at Mercury's dayside surface. These particles can be neglected in the context of this paper since they reach a maximum altitude of ∼60 km and, when ionized, mainly reimpact the dayside surface without being significantly energized. Photo-stimulated desorption, micro-meteoritic vaporization and solar wind sputtering at high latitudes were treated independently, considering typical ejection rates from Mercury's surface and a uniform spatial distribution of the ejecta for micro-meteoritic vaporization and photo-stimulated desorption (Leblanc and Johnson, 2002). No depletion of the sodium density at the surface was considered. Also, because of the pronounced eccentricity of Mercury's orbit, the solar wind, photon flux, micro-meteoritic flux, solar radiation pressure and ionization frequency, all significantly differ at perihelion and aphelion. This led us to consider the two cases separately.

The model exosphere used as the source of Na^+ ions is shown in Fig. 3, which presents color-coded sodium densities in the noon-midnight meridian plane (top panels), as well as in the equatorial plane (bottom panels). Note that only particles that are susceptible to circulate inside Mercury's magnetosphere (that is, that are located inside the hermean magnetopause) were considered in this figure, so that the pattern displayed in Fig. 3 does not have a spherical shape. Figure 3 displays significant (above 10 cm^{-3} at perihelion) densities near the planet's surface in the dayside sector, as well as a rapid decrease with increasing altitude. Note that, because we neglect the very low energy component due to thermal desorption, these density levels are much smaller than the near-surface density in the subsolar region deduced from observations, which is of the order of 10^4 cm^{-3}. Also, in the right panels of Fig. 3, weaker Na densities can be seen at aphelion, due to weaker photon and solar wind fluxes.

The magnetospheric circulation of Na^+ ions produced via ionization of exospheric neutrals was then investigated by attributing a test particle to each bin in Fig. 3. Initial pitch angles and energies for the test particles were those obtained from Monte Carlo simulations. The flow rate (in ions.s^{-1}) attributed to a test particle associated with a given bin labeled i was taken as $F_i = f_{\rm ion} N_i V_i$, where $f_{\rm ion}$, N_i, and V_i are the ionization frequency, bin density, and bin volume, respectively. Subsequently, all test particles (except those originating from the shadow region in the nightside sector for which one has $f_{\rm ion} = 0$) were traced in the electric and magnetic field models described in Sect. 2, and according to a magnetospheric grid featuring cubic bins of 0.1 R_M edge. Once the trajectory calculations were performed, the plasma parameters in a given bin were calculated by summation over the various test ions passing through that bin. More specif-

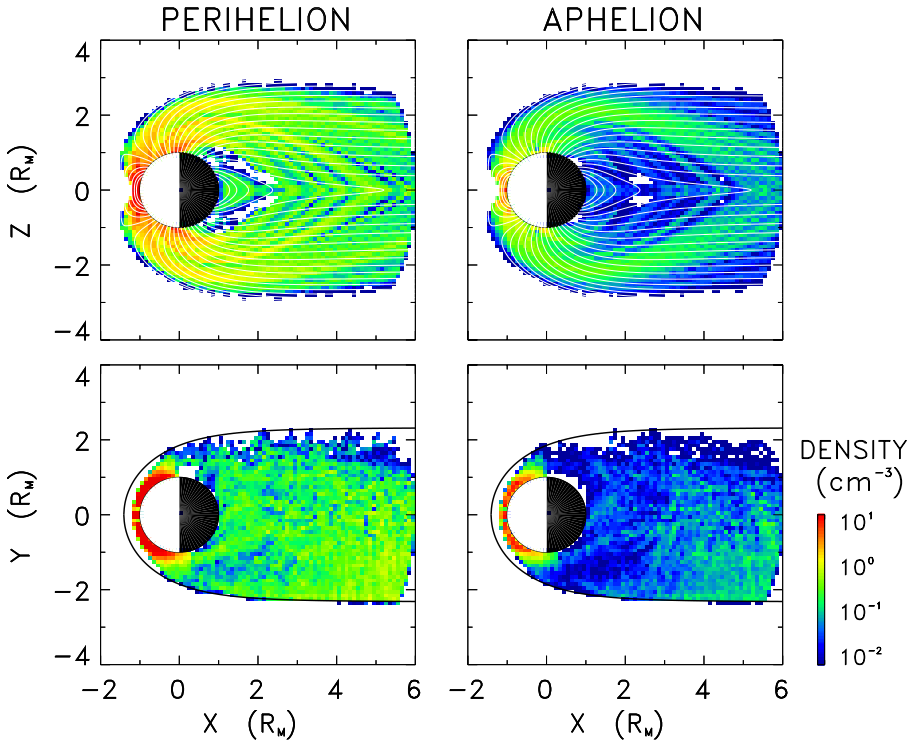

Fig. 4. Model density of Na^+ ions at (left) perihelion and (right) aphelion. Top and bottom panels show cross sections in the noon-midnight meridian plane and the equatorial plane, respectively. The density is coded according to the color scale at the right.

ically, given a three-dimensional bin labeled with indices (j_X, j_Y, j_Z) and denoting the particle residence time within that bin by Δt, the volume of the bin by ϑ, the particle energy by ε and the time of flight by T, one has

$$\eta(j_X, j_Y, j_Z) = \frac{\sum_i F\Delta t}{\vartheta} \tag{3a}$$

$$\langle\varepsilon(j_X, j_Y, j_Z)\rangle = \frac{\sum_i F\Delta t\varepsilon}{\sum_i F\Delta t} \tag{3b}$$

$$\langle T(j_X, j_Y, j_Z)\rangle = \frac{\sum_i F\Delta t T}{\sum_i F\Delta t}, \tag{3c}$$

where, η, $\langle\varepsilon\rangle$, and $\langle T\rangle$ are the ion density, the mean kinetic energy, and the mean time of flight, respectively.

Figure 4 shows the results obtained for the Na^+ density. In this figure, as well as in the following figures, the results of the computations are presented both in the noon-midnight meridian plane (top panels) and in the equatorial plane (bottom), at perihelion (left) and at aphelion (right). These results are coded according to the color scale on the right. Note that the patterns obtained are symmetrical with respect to the equator, since identical sources were considered in the Northern and Southern Hemispheres. A striking feature in Fig. 4 is the significant density levels that are present at perihelion. Indeed, on average, the bottom left panel of Fig. 4 exhibits density levels of the order of several tenths cm^{-3} in the equatorial nightside magnetosphere, that is, levels which are quite comparable to those encountered in the Earth's plasma sheet. This stresses the importance of composition measurements at Mercury, as envisaged, for example, in the mass spectrometer analyzer to be proposed for the Bepi Colombo mission. The bottom left panel of Fig. 4 also displays a prominent dawn-dusk asymmetry, with a density accumulation in the dusk flank tailward of the $\kappa \sim 1$ domain (see Fig. 1). At aphelion (right panels of Fig. 4), the computed density levels are significantly smaller (by about one order of magnitude), as expected from the less dense exosphere (Fig. 3). Note finally the very large densities obtained in the frontside sector near the planet's surface, of the order of $10\,cm^{-3}$.

In the top panels of Fig. 4, distinct streaks of enhanced densities can also be seen. Equation (3a) indicates that such density enhancements may follow either from large flow rates or from large residence times. In order to explore this issue further, Fig. 5 presents the Na^+ density, average time of flight, and average energy as a function of X distance in the midnight meridian plane. These profiles are shown at perihelion, at a Z height of $0.5\,R_M$. In the top panel of Fig. 5, one can recognize the distinct density streaks displayed in the upper left panel of Fig. 4. By comparison with the bottom panels of Fig. 5, it can be seen that, in some cases (e.g. near $X = 5\,R_M$), a density decrease coincides with a smaller time of flight and a larger energy. In such cases, the residence time Δt clearly plays a role in the computed density fluctuations. Overall, however, no clear correlation can be seen in Fig. 5 between the computed density and the time of flight, which suggests that most of the density fluctuations in

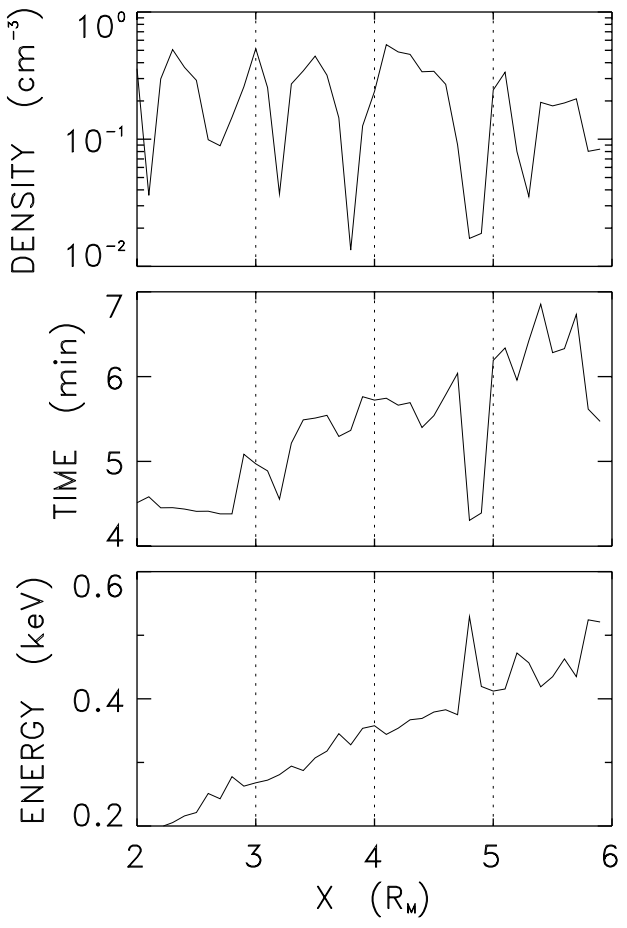

Fig. 5. (top) Computed Na^+ density, (center) average time of flight, and (bottom) average energy as a function of X distance for $Y = 0$ and $Z = 0.5\,R_M$.

Fig. 4 are due to different statistical weights of the test particles. The details of the density pattern in Fig. 4 thus depend on the model exosphere considered, and we may speculate that different initial conditions will lead to some differences in the distribution obtained, however, without affecting significantly the average contribution.

In the top panels of Fig. 4, some empty bins are noticeable in the near-tail. These result from the grid adopted in the simulations, and a refined sampling at ejection into the magnetosphere will likely yield an improved coverage of this region of space. Empty bins can be seen as well in the dawn flank of the magnetosphere (bottom panels of Fig. 4), which contrasts with the fairly regular filling obtained in the dusk flank. Rather than a consequence of the sampling adopted, this latter asymmetry follows from the ion drift direction, that is, any given point of the dusk magnetopause can be connected to a given ion drift path inside the magnetosphere, whereas this is not the case at the dawn magnetopause. The irregular boundary layer that is achieved at low latitudes in the dawn flank (bottom panels of Fig. 4) thus does not appear to be an artifact of the numerical simulations and is actually reminiscent of the structure put forward by Christon (1989).

Further insights into the Na^+ dynamics at Mercury may be obtained from Figs. 6 and 7, which show the computed time of flights and energies using a format similar to that of Fig. 4. It can be seen in Fig. 6 that, as one progresses from high to low latitudes over the polar cap, the ion residence time gradually increases up to several minutes. Note the enhanced residence time in the immediate vicinity of the planet at low latitudes, due to particles that are convected back into the inner magnetosphere. In Fig. 7, it is also apparent that the dense population at low latitudes in the frontside sector has average energies of $\sim$10 eV or below, that is, in a range comparable to that of the exospheric source. This contrasts with the keV population obtained in the equatorial magnetotail. Because ions are accelerated during duskward drift along the convection electric field (see Fig. 2), a pronounced asymmetry between dawn and dusk sectors is noticeable, with mean energies of the order of a few hundreds of eV and several keV, respectively. In addition, the bottom panels of Fig. 7 show no energetic Na^+ that are trapped near the equator in the dayside magnetosphere, or equivalently no indication of ring current development. As mentioned above, because of their large Larmor radii, most Na^+ that travel tailward of 2–3 R_M intercept the dusk magnetopause upon interaction with the tail current sheet, so that only a limited fraction of the exospheric ions have access to the dayside region from the magnetotail (see, e.g. Fig. 2). For these latter ions, pitch-angle scattering at $\kappa < 3$ (Fig. 1) leads to injection into the loss cone, which hampers stable trapping at low latitudes.

Finally, it is apparent from the top panels of Fig. 7 that, in contrast to the innermost region, only a thin (a few tenths of R_M) sheet of energetic Na^+ is obtained tailward of 3 R_M. This is due to the encounter of the dusk magnetopause during meandering motion about the midplane, so that ions cannot escape from the equatorial region and deposit densities at higher latitudes. Also of interest are the energy variations obtained in the magnetospheric lobes. As mentioned above (Sect. 3), the centrifugal acceleration due to the $\boldsymbol{E} \times \boldsymbol{B}$ drift path curvature during transport from high to low latitudes is more efficient at Mercury than at Earth (Delcourt et al., 2002). In accordance with this, the top panels of Fig. 7 exhibit a sharp ion energy gradient in the magnetospheric lobes, with energy variations from a few eVs or a few tens of eV near the planet's surface, up to a few hundreds of eV above $\sim$1 R_M altitude. Note, moreover, the thin layer of energetic Na^+ adjacent to the high-latitude magnetopause due to enhanced energization in the outer cusp region.

4 Energetic Na^+ precipitation at Mercury

It has been suggested in previous studies that bombardment by energetic particles from the magnetosphere may yield further ejection of material from Mercury's surface, which will add to meteoroid impacts and sputtering processes (e.g. Potter and Morgan, 1990). In particular, the test particle analysis of Ip (1993) suggested substantial recycling of exospheric Na^+, with precipitation of low-energy ions at high

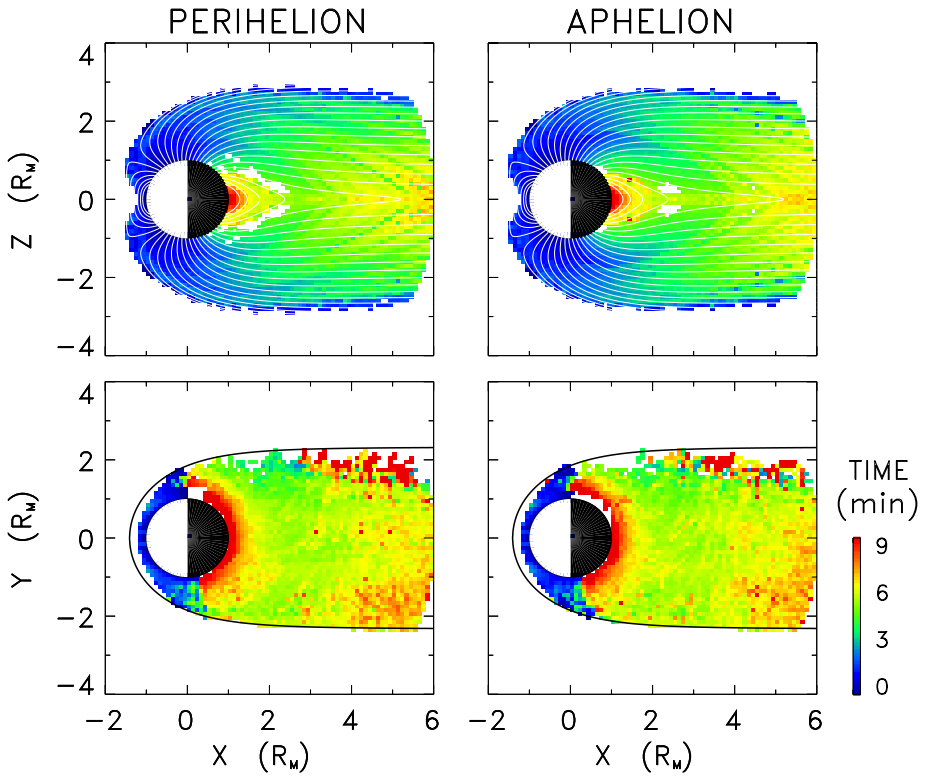

Fig. 6. As for Fig. 4 but for the Na^+ ion average time of flight.

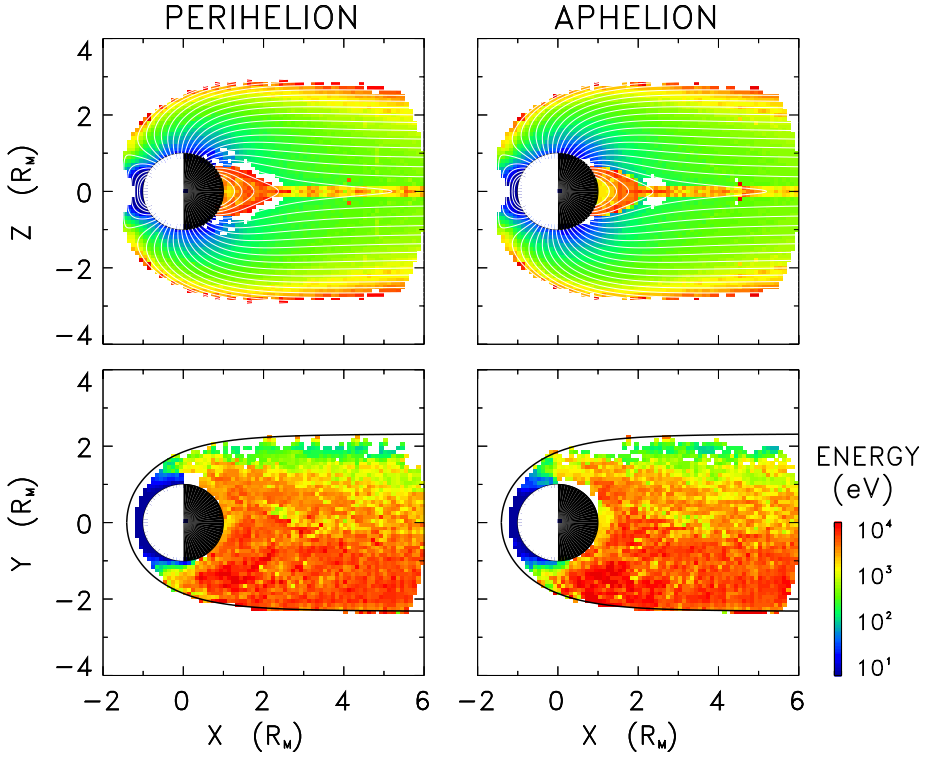

Fig. 7. As for Fig. 4 but for the Na^+ ion average energy.

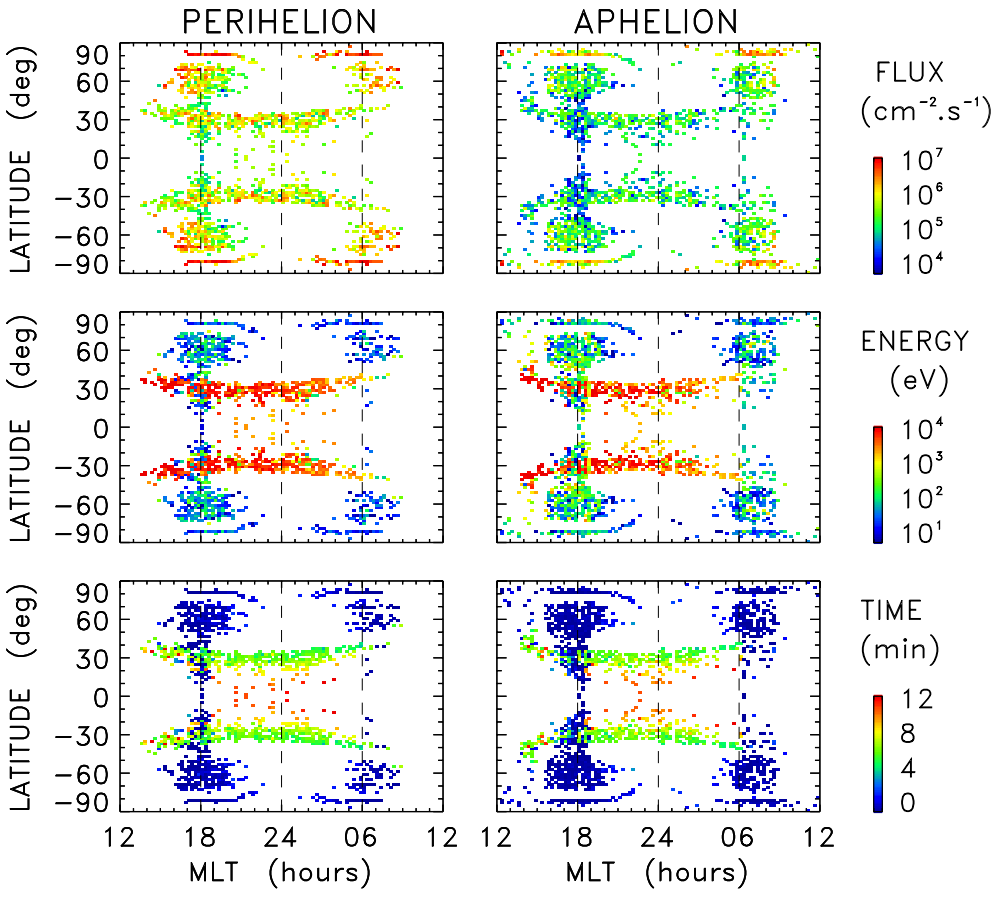

Fig. 8. Characteristics of precipitating Na^+ ions at (left) perihelion and (right) aphelion. The panels from top to bottom show the color-coded ion flux, average energy, and residence time in the magnetosphere.

latitudes in the pre-dawn sector and high-energy ones at lower latitudes in the nightside sector (see e.g. Fig. 4 of that study). The non-adiabatic behavior of heavy ions in the near-tail is of paramount importance in this context. Indeed, several studies dedicated to analysis of particle dynamics in a field reversal when κ is of the order of unity (e.g. Sergeev et al., 1983; Zelenyi et al., 1990; Delcourt et al., 1996) demonstrated that this regime is characterized by chaotic pitch-angle scattering, which leads to prominent injections into the loss cone and subsequent precipitation. At Earth, Sergeev et al. (1993) identified the equatorward boundary (referred to as the "isotropic boundary") of this latter precipitation as the downstream image of the inward limit of nonadiabatic motion in the inner plasma sheet. Knowledge of this auroral boundary then allows for remote sensing of the magnetotail magnetic field. On the other hand, for $\kappa < 1$, quasi-adiabatic (Speiser-type) behavior, which is characterized by negligible magnetic moment change, becomes possible, so that ions originating from low altitudes (i.e. the strong B region) can travel back to such altitudes after interaction with the magnetotail current sheet. Be it via chaotic pitch angle scattering or resonant interaction with the neutral sheet, we expect a significant flux of downflowing Na^+ at Mercury, since one has $\kappa < 3$ throughout most of the magnetotail (Fig. 1). On the other hand, because of the large Na^+ Larmor radii and consequent ion loss at the dusk magnetopause beyond $\sim 3\,R_M$ (Fig. 2), we expect the downflowing ion flux to be limited in latitudinal extent.

The results of the trajectory computations confirm these expectations, as illustrated in Fig. 8. In this figure, the color-coded Na^+ flux, average energy and time of flight at impact onto the planet's surface are shown as a function of both longitude and latitude, at perihelion (left) and at aphelion (right). A striking feature in Fig. 8 is the existence of two bands of Na^+ impacts at mid-latitudes. These bands are obtained at nearly all longitudes, with the exception of the cusp region in the frontside sector. Because identical upflows were considered in the Northern and Southern Hemispheres, these bands also are symmetrical about the equator. They extend over 10°–20° near 30° latitude in the midnight sector and occur at gradually higher latitudes as one progresses toward the dayside sector. Downflowing ions in these bands have energies in the keV range (center panels of Fig. 8). Their flux is of the order of $10^6\,cm^{-2}\,s^{-1}$ at perihelion, and smaller by about one order of magnitude at aphelion. In the bottom panels of Fig. 8, note the mean residence times in the magnetosphere, which are of the order of 4 to 6 min.

Figure 8 also exhibits significant impacts of low-energy

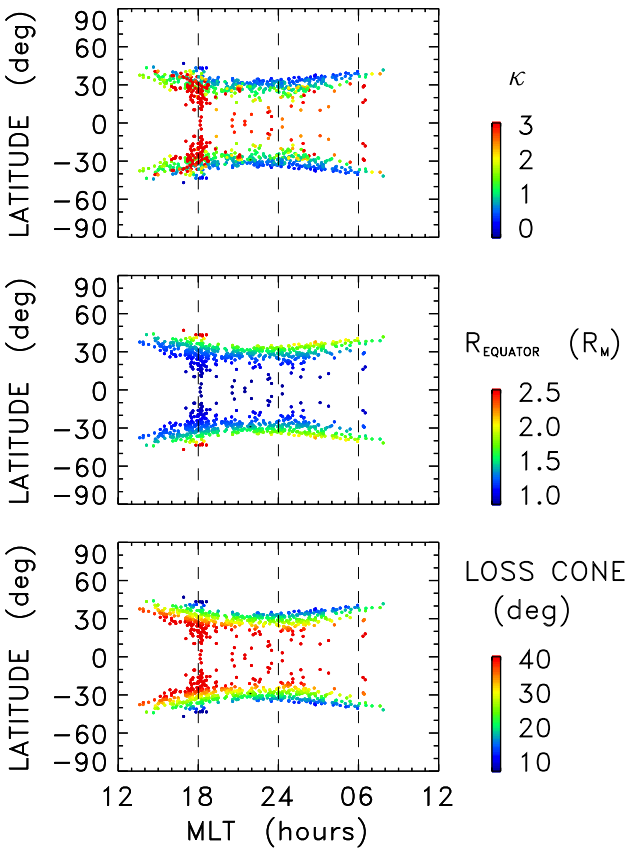

Fig. 9. (from top to bottom) The κ parameter, equatorial crossing distance, and loss cone for the precipitating Na^+ shown at left in Fig. 8.

Na^+ at high latitudes in the terminator region, with flux levels that are comparable to those in the mid-latitude precipitation region. As expected from their low energies (center panels) and short times of flight (bottom panels), these latter ions have not circulated within the magnetosphere and actually correspond to the downflowing part of the initial exospheric population. Note that none of these low-energy ions are recorded in the noon and midnight sectors because of the rapid $\boldsymbol{E} \times \boldsymbol{B}$ transport in the antisunward direction. Comparison of Fig. 8 with the study of Ip (1993) reveals significant differences in the precipitation patterns obtained, likely due to the different modeling techniques adopted. Nevertheless, there exist robust features such as the mean Na^+ energy variation as a function of longitude.

The two bands of downflowing energetic Na^+ in Fig. 8 are reminiscent of auroral precipitation at Earth. They can be better appreciated in Fig. 9 which shows the equatorial crossing distance immediately before precipitation (center panel), the κ parameter calculated at this latter distance (top panel), as well as the width of the loss cone at this distance as derived from magnetic moment conservation: $\alpha_{LC} = \arcsin(B_{EQ}/B_P)^{1/2}$ (here, B_{EQ} and B_P denote the magnetic field magnitudes at the equatorial foot and planetary foot of the field line, respectively). Only the perihelion case is shown in Fig. 9. Note that the low-energy ions obtained at high latitudes in Fig. 8 are absent since they do not cross the equator. It is apparent from the center panel of Fig. 9 that all downflowing Na^+ originate from equatorial distances smaller than $\sim 2.5\, R_M$. As described above, at further distances, ions have such large Larmor radii that they reach the dusk flank during their Z-oscillation about the midplane. In other words, in contrast to Earth, where particle precipitation is limited by the polar cap on the poleward side, the poleward boundary of the precipitation bands in Fig. 8 coincides with the limit of slow gyromotion about the magnetic field component normal to the midplane. Figure 9 indicates that, in these bands, κ varies from ~ 1 at the equatorward boundary (i.e. here, precipitation follows from pitch-angle scattering into the large loss cone) down to the first energy resonances ($\kappa \sim 0.1$–0.5) at the poleward boundary (here, precipitation results from quasi-adiabatic motion inside the neutral sheet).

Figures 8 and 9 demonstrate a specific feature of the small-scale Mercury's magnetosphere. Indeed, numerous observations at Earth have revealed that different ion species ejected from the high-latitude dayside ionosphere are dispersed over the polar cap under the effect of the large-scale magnetospheric convection. This velocity filter was referred to as the "large-scale geomagnetic mass spectrometer" effect because of its similarity to the principle of operation of a magnetic mass spectrometer (e.g. Lockwood et al., 1985; Moore et al., 1985). Figure 10 presents the trajectories of H^+ and Na^+ ions launched into the hermean magnetosphere with 1 eV energy from 65° invariant latitude on the noon meridian. Not surprisingly, the trajectory projections in the noon-midnight meridian plane (top panel of Fig. 10) indicate that the above velocity filter effect is also at work at Mercury, namely: because of its smaller parallel speed, the Na^+ ion is convected into lower L-shells and does not travel as far in the magnetotail as the proton. On the other hand, the trajectory projections in the equatorial plane (bottom panel of Fig. 10) reveal that the large-scale hermeomagnetic mass spectrometer is complicated by an additional gyroradius filter effect. Whereas the Na^+ ion does not travel back toward the planet because it intercepts the magnetopause during its meandering motion about the midplane (see also Fig. 2), the proton that travels further out into the magnetotail (up to $\sim 5\, R_M$) has a smaller Larmor radius and can execute a full Speiser orbit before returning to low altitudes. After energization up to 4 keV, this proton ultimately impacts the planet's surface at a latitude of $\sim 40°$, which is inaccessible to the Na^+ ion. Note that both test particles have $\kappa \approx 0.2$, i.e. of the order of the third resonance. In other words, since the precipitation bands in Fig. 8 are controlled by non-adiabatic motion in the magnetotail, we expect them to significantly depend on ion species and to extend at higher latitudes and lower energies for smaller mass-to-charge ratios.

Though narrowly localized in latitude, the pattern obtained in Fig. 8 suggests that energetic ions precipitating from the magnetosphere may play a role in the ejection of planetary material, as initially suggested by Potter and Morgan (1990).

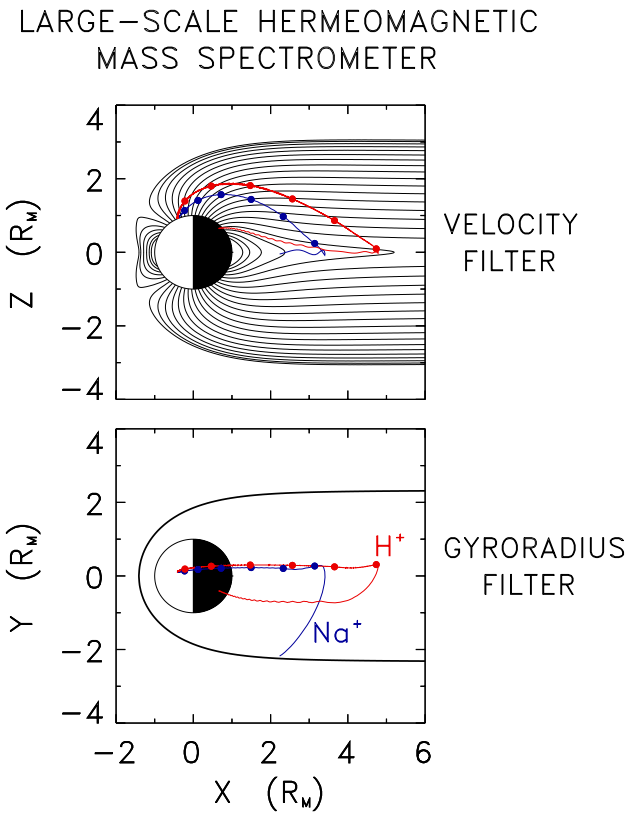

Fig. 10. Model trajectories of (red) H^+ and (blue) Na^+ ions. Top and bottom panels show the trajectory projections in the noon-midnight meridian plane and in the equatorial plane, respectively. The ions are launched from the same position with identical energies and pitch angles. Closed circles show the time of flight by steps of one minute.

In particular, it may be speculated that, during events of enhanced coupling between the magnetosphere and the solar wind, an increased convection rate will lead to further confinement and energization of planetary ions inside Mercury's magnetosphere, and hence, to enhanced ion precipitation. Regarding the low-energy downflowing ions at high latitudes, these may subsequently enhance the exosphere content via recycling in surface material.

In order to obtain some insights into this additional sputtering process, we computed first-order estimates of the flux of neutral atoms ejected by the downflowing Na^+ in Fig. 8. As in Fig. 3, some of these sputtered particles may just follow ballistic trajectories and fall back to the planet's surface whereas others will escape depending on their initial energy. The distribution of particles sputtered with ejection energy E_E can be expressed as (Sieveka and Johnson, 1984):

$$F(E_E) \sim \frac{E_E}{(E_E + E_B)^3} \left[1 - \left(\frac{E_E + E_B}{E_I} \right)^{1/2} \right], \qquad (4)$$

where E_I is the energy of the incident particle and E_B is the surface binding energy of the sputtered particle. The products arising from particle bombardment depend both on the composition and on the chemical structure of the planet's surface. In the case of Mercury, the presence of various neutral species (H, O, Na, K, Ca) in the exosphere has been established by both space and ground-based observations (e.g. Potter and Morgan, 1986; Bida et al., 2000). Though the downflowing Na^+ in Fig. 8 may lead to ejection of distinct species into the magnetosphere, we here restrict our analysis to the production of sodium atoms.

Figure 11 shows the omnidirectional Na flux obtained using the results of Fig. 8, and considering an average ion-sputter yield of 0.35 for the incident ions (e.g. Lammer et al., 2002). Assuming a sodium composition of the hermean surface of 0.53% (e.g. Killen et al., 2001) and taking a binding energy of 2 eV (e.g. McGrath et al., 1986), the flux in Fig. 11 was obtained by integrating the energy distribution (4) within three energy intervals: 1–10 eV, 10–100 eV, 100 eV–1 keV. Only the perihelion case (upper left panel of Fig. 8) was considered. In Fig. 11, one recognizes the precipitation pattern displayed in Fig. 8, with Na flux of the order of 10^3–10^4 cm^{-2} s^{-1}. This is 3 to 4 orders of magnitude smaller than the flux due to solar wind protons (e.g. Leblanc and Johnson, 2002; Massetti et al., 2002). However, the sputtering due to solar wind and that due to energetic magnetospheric ions are effective in quite distinct regions, namely: at high latitudes in the dayside sector in the former case and within an extended rim at mid-latitudes in the latter case. A crude estimate of the flow rate in the nightside sector in Fig. 11 yields 10^{20}–10^{21} s^{-1} for only sodium atoms. As mentioned above, it is likely that the total production of neutrals (e.g. O, K, Ca) is significantly larger. It thus appears that sputtering due to ion precipitation from the magnetosphere may play a specific role in refilling of the exosphere and erosion of the planet's surface, an issue that will be addressed by the neutral particle analyzer to be proposed for the Bepi Colombo mission.

5 Conclusions

The numerical simulations performed provide insights into the behavior of Na^+ ions of planetary origin at Mercury. Within the limits of the model, the simulations reveal several features of interest that are linked to the small spatial scales of the hermean magnetosphere. First, because of the pronounced curvature of the $\boldsymbol{E} \times \boldsymbol{B}$ drift paths, significant centrifugal acceleration occurs during transport from high to low latitudes, so that the magnetospheric lobe content is found to be significantly more energetic (several hundreds of eV) at Mercury than at Earth. The simulations also emphasize the prominent role of finite Larmor radius effects. Ions with large mass-to-charge ratios such as Na^+ are found to behave non-adiabatically throughout most of the hermean magnetosphere. In the innermost region (typically, within 2 R_M radial distance), this non-adiabatic behavior is characterized by prominent pitch-angle scattering ($\kappa \sim 1$), which hampers stable trapping at low latitudes. At larger distances, quasi-adiabatic (Speiser-type) behavior may occur, together with significant (several keV) ion energization. The net result of

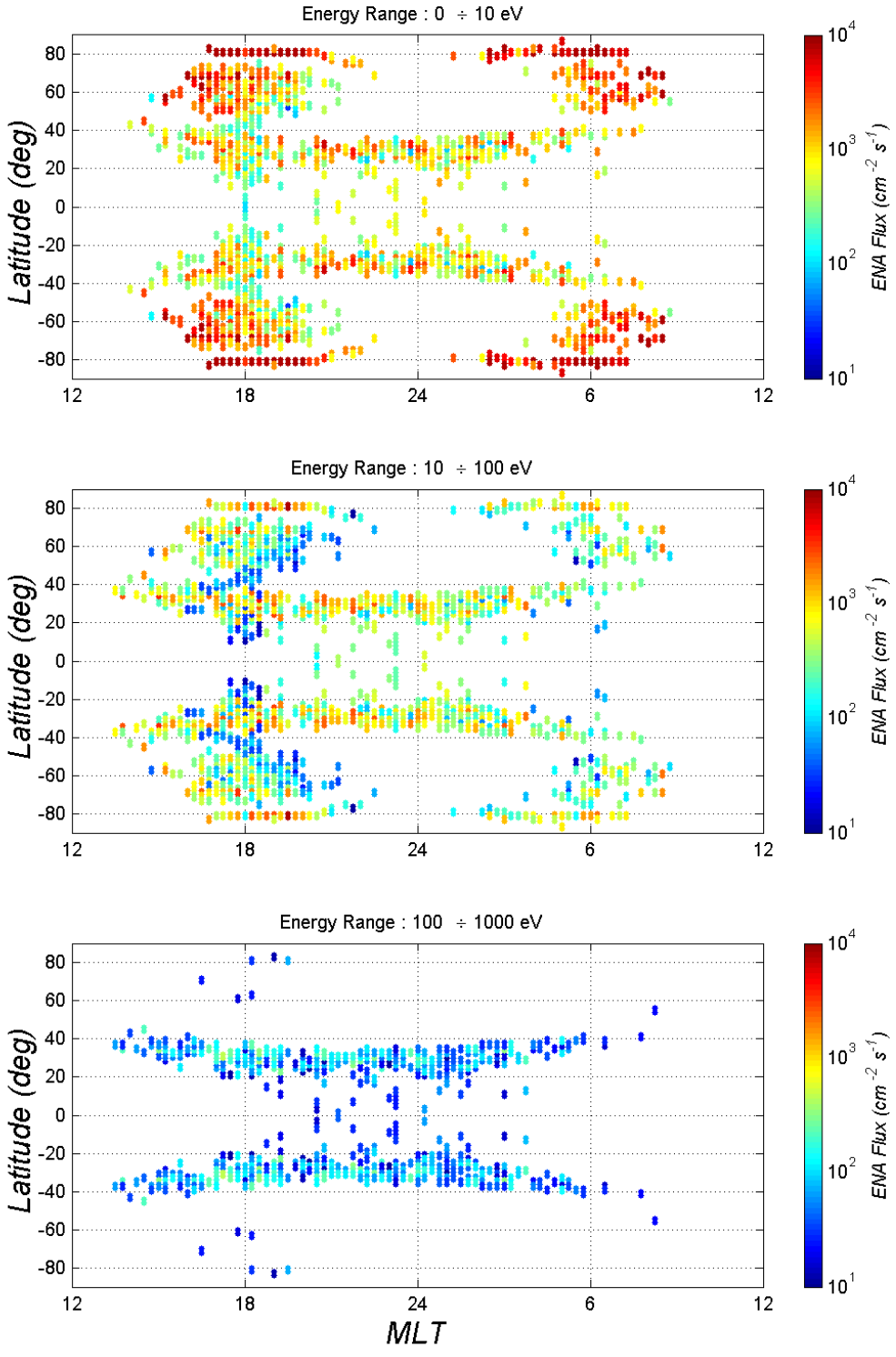

Fig. 11. Flux of sodium atoms due to Na^+ ions precipitating from the magnetosphere at perihelion (left panels of Fig. 8). The neutral atom flux is shown in three different energy ranges: (from top to bottom) 0–10 eV, 10–100 eV, 100 eV–1 keV.

this non-adiabatic circulation is a quite substantial filling (up to a few tenths cm^{-3} at perihelion) of the inner tail and a thin sheet of energetic Na^+ ions at larger distances. Due to a less dense exosphere, the density contributed by planetary ions is found to be smaller at aphelion. Also, the non-adiabatic motion of ions in the magnetotail is responsible for a narrow band of energetic precipitation in each hemisphere at the planet's surface. These bands, which extend over several degrees in latitude and a wide range of longitude, likely lead to additional sputtering of planetary material. The poleward

boundary of these bands corresponds to the limit of slow gyromotion in the magnetotail and thus depends on ion species. This latter gyroradius filter effect forms a specific feature of the large-scale magnetic mass spectrometer at Mercury.

Acknowledgements. Topical Editor T. Pulkkinen thanks S. W. H. Cowley for his help in evaluating this paper.

References

Baker, D. N., Simpson, J. A., and Eraker, J. H.: A model of impulsive acceleration and transport of energetic particles in Mercury's magnetosphere, J. Geophys. Res., 91, 8742–8748, 1986.

Bida, T. A., Killen, R. M., and Morgan, T. H.: Discovery of calcium in Mercury's atmosphere, Nature 404, 159–161, 2000.

Büchner, J. and Zelenyi, L. M.: Regular and chaotic charged particle motion in magnetotaillike field reversals: 1. Basic theory of trapped motion, J. Geophys. Res., 94, 11 821–11 842, 1989.

Burkhart, G. R. and Chen, J.: Differential memory in the Earth's magnetotail, J. Geophys. Res., 96, 14 033–14 049, 1991.

Chen, J. and Palmadesso, P. J.: Chaos and nonlinear dynamics of single-particle orbits in magnetotaillike magnetic field, J. Geophys. Res., 91, 1499–1508, 1986.

Christon, S. P., Feynman, J., and Slavin, J. A.: Dynamic substorm injections: Similar magnetospheric phenomena at Earth and Mercury, AGU Monograph on "Magnetotail Physics", 393, 1987.

Christon, S. P.: Plasma and energetic electron flux variations in the Mercury 1 C event: Evidence for a magnetospheric boundary layer, J. Geophys. Res., 94, 6481–6505, 1989.

Cladis, J. B.: Parallel acceleration and transport of ions from polar ionosphere to plasma sheet, Geophys. Res. Lett., 13, 893–896, 1986.

Daglis, I. A. and Axford, W. I.: Fast ionospheric response to enhanced activity in geospace: Ion feeding of the inner magnetotail, J. Geophys. Res., 101, 5047–5066, 1996.

Delcourt, D. C., Moore, T. E., Orsini, S., Millilo, A., and Sauvaud, J.-A.: Centrifugal acceleration of ions near Mercury, Geophys. Res. Lett., 29 (12), 10.1029/2001GL013829, 2002.

Delcourt, D. C., Sauvaud, J.-A., Martin, Jr., R. F., and Moore, T. E.: On the nonadiabatic precipitation of ions from the near-Earth plasma sheet, J. Geophys. Res., 101, 17 409–17 418, 1996.

Delcourt, D. C., Martin, R. F., and Alem, F.: A simple model of magnetic moment scattering in a field reversal, Geophys. Res. Lett., 21, 1543–1546, 1994.

Delcourt, D. C., Chappell, C. R., Moore, T. E., and Waite, Jr., J. H.: A three-dimensional numerical model of ionospheric plasma in the magnetosphere, J. Geophys. Res., 94, 11 893–11 920, 1989.

Glassmeier, K.-H.: The hermean magnetosphere and its ionosphere-magnetosphere coupling, Planet. Space Sci., 45, 119–125, 1997.

Goldstein, B. E., Suess, S. T., and Walker, R. J.: Mercury: Magnetospheric processes and the atmospheric supply and loss rates, J. Geophys. Res., 86, 5485–5499, 1981.

Hamilton, D. C., Gloeckler, G., Ipavich, F. M., Stüdemann, W., Wilken, B., and Kremser, G.: Ring current development during the great geomagnetic storm of February 1986, J. Geophys. Res., 93, 14 343–14 355, 1988.

Ip, W.-H.: On the surface sputtering effects of magnetospheric charged particles at Mercury, Astrophys. J., 418, 451–456, 1993.

Ip, W.-H.: Dynamics of electrons and heavy ions in Mercury's magnetosphere, Icarus, 71, 441–447, 1987.

Johnson, R. E.: Energetic charge-particle interactions with atmospheres and surfaces, Springer-Verlag, New York, 1990.

Kabin, K., Gombosi, T. I., De Zeeuw, D. L., and Powell, K. G.: Interaction of Mercury with the solar wind, Icarus, 143, 397–406, 2000.

Kallio, E. and Janhunen, P.: Modeling the solar wind interaction with Mercury by a quasineutral hybrid model, Ann. Geophysicae, in press, 2003.

Killen, R. M., Potter, A. E., Reiff, P. H., Sarantos, M., Jackson, B. V., Hick, P., and Giles, B. L.: Evidence for space weather at Mercury, J. Geophys. Res., 106, 20 509–20 526, 2001.

Lammer, H., Wurz, P., Patel, M. R., Killen, R., Kolb, C., Massetti, S., Orsini, S., and Milillo, A.: The variability of Mercury's exosphere by particle and radiation induced surface release processes, Icarus, submitted, 2002.

Leblanc, F. and Johnson, R. E.: Neutral sodium Mercury's exosphere, Icarus, submitted, 2002.

Lockwood, M., Moore, T. E., Waite, Jr., J. H., Chappell, C. R., Horwitz, J. L., and Heelis, R. A.: The geomagnetic mass spectrometer – Mass and energy dispersions of ionospheric flows into the magnetosphere, Nature, 316, 612–613, 1985.

Luhmann, J. G., Russell, C. T., and Tsyganenko, N. A.: Disturbances in Mercury's magnetosphere: Are the Mariner 10 "substorms" simply driven, J. Geophys. Res., 103, 9113–9120, 1998.

Luhmann, J. G. and Friesen, L. M.: A simple model of the magnetosphere, J. Geophys. Res., 84, 4405–4408, 1979.

Massetti, S., Orsini, S., Milillo, A., Mura, A., De Angelis, E., Lammer, H., and Wurz, P.: Mapping of the cusp plasma precipitation on the surface of Mercury, Icarus, submitted, 2002.

McGrath, M. A., Johnson, R. E., and Lanzerotti, L. J.: Sputtering of sodium on the planet Mercury, Nature, 323, 694–696, 1986.

Moore, T. E., Chandler, M. O., Fok, M.-C., Giles, B. L., Delcourt, D. C., Horwitz, J. L., and Pollock, C. J.: Ring currents and internal plasma sources, Space Sci. Rev., 95, 555–568, 2001.

Moore, T. E., Peterson, W. K., Russell, C. T., Chandler, M. O., Collier, M. R., Collin, H. L., Craven, P. D., Fitzenreiter, R., Giles, B. L., and Pollock, C. J.: Ionospheric mass ejection in response to a CME, Geophys. Res. Lett., 26, 2339–2342, 1999.

Moore, T. E., Chappell, C. R., Lockwood, M., and Waite, Jr., J. H.: Superthermal ion signatures of auroral acceleration processes, J. Geophys. Res., 90, 1611–1618, 1985.

Northrop, T. G.: The adiabatic motion of charged particles, Wiley Interscience, New York, 1963.

Potter, A. E. and Morgan, T. H.: Evidence for magnetospheric effects on the sodium atmosphere of Mercury, Science, 248, 835–838, 1990.

Potter, A. E. and Morgan, T. H.: Potassium in the atmosphere of Mercury, Icarus, 67, 336–340, 1986.

Potter, A. E. and Morgan, T. H.: Discovery of sodium in the atmosphere of Mercury, Science, 229, 651–653, 1985.

Roederer, J. G.: Dynamics of geomagnetically trapped radiation, Physics and chemistry in space, Springer, New York, 1970.

Sergeev, V. A., Malkov, M., and Mursula, K.: Testing the isotropic boundary algorithm method to evaluate the magnetic field configuration in the tail, J. Geophys. Res., 98, 7609–7620, 1993.

Sergeev, V. A., Sazhina, E. M., Tsyganenko, N. A., Lundblad, J. A., and Soraas, F.: Pitch-angle scattering of energetic protons in the magnetotail current sheet as the dominant source of their siotropic precipitation into the nightside ionosphere, Planet. Space Sci., 31, 1147–1155, 1983.

Sieveka, E. M. and Johnson, R. E.: Ejection of atoms and molecules from Io by plasma-ion impact, Astrophys. J., 287, 418–426,

1984.

Speiser, T. W.: Particle trajectory in model current sheets, 1, Analytical solutions, J. Geophys. Res., 70, 4219–4225, 1965.

Taktakishvili, A. L. and Zelenyi, L. M.: Inductive acceleration of protons and electrons in planetary magnetotails, Proc. of International Workshop on "Reconnection in space plasmas", ESA-SP, 285, 227–232, 1988.

Tsyganenko, N. A.: Effects of the solar wind conditions on the global magnetospheric configuration as deduced from data-based models, Proc. of Third International Conference on Substorms (ICS-3), ESA-SP, 389, 181–185, 1996.

Volland, H.: A model of the magnetospheric convection electric field, J. Geophys. Res., 83, 2695–2699, 1978.

Whang, Y. C.: Magnetospheric magnetic field of Mercury, J. Geophys. Res., 82, 1014–1030, 1977.

Yau, A. W., Shelley, E. G., Peterson, W. K., and Lenchyshyn, L.: Energetic auroral and polar ion outflow at DE-1 altitudes: magnitude, composition, magnetic activity dependence, and long-term variations, J. Geophys. Res., 90, 8417–8432, 1985.

Zelenyi, L. M., Galeev, A., and Kennel, C. F.: Ion precipitation from the inner plasma sheet due to stochastic diffusion, J. Geophys. Res., 95, 3871–3882, 1990.